Rayleigh pulse - dynamic triggering of fault slip

by

K. Uenishi*, H.P. Rossmanith

Institute of Mechanics, Vienna University of Technology, Austria

and

A.E. Scheidegger

Institute of Theoretical Geodesy and Geophysics, Vienna University of Technology, Austria

* Present address: Department of Architecture and Civil Engineering, Kobe University, Japan

Bulletin of the Seismological Society of America, Vol.89(5), pp.1296-1312,

1999.

ABSTRACT

We present an experimental and numerical investigation of the interaction of a Rayleigh (R-) pulse with a partially contacting strike-slip fault between similar and dissimilar materials. This study is intended to offer an improved understanding of the earthquake rupture mechanisms. The fault is subjected to static normal and shear pre-stresses. Utilizing two-dimensional dynamic photoelasticity in conjunction with high-speed cinematography, the evolution of time-dependent isochromatic fringe patterns (contours of maximum in-plane shear stress) associated with Rayleigh pulse-fault interaction is experimentally recorded. It is shown that fault slip (instability) can be triggered by a pulse that propagates along the fault interface at Rayleigh wave speed (about 90% of the relevant shear wave speed), and that the direction of the static shear pre-loading has an influence on the initiation of fault slip. For the numerical studies, a finite-difference wave propagation simulator SWIFD (**S**olids·**W**ave·**I**mpact·**F**racture·**D**amage) is used for a quantitative analysis of the problem under different combinations of contacting materials. Dynamic rupture in laterally heterogeneous structures is discussed by considering the effect of the acoustic impedance ratio of the two contacting materials on the wave patterns. The results indicate that upon fault rupture, Mach (head) waves, which carry a relatively large amount of concentrated energy, can be generated that propagate from the fault contact region into the acoustically softer material. Such Mach waves can cause concentrated damage in a particular region located inside an adjacent acoustically softer area. This type of damage concentration might be another possible reason for the generation of the "damage belt" in Kobe, Japan, on the occasion of the 1995 Hyogo-ken Nanbu earthquake.

Keywords: Acoustic impedance ratio, Contact mechanics, Dynamic faulting, Dynamic photoelasticity, Earthquake dynamics; Earthquake rupture mechanism, Finite difference method, Hyogo-ken Nanbu (Kobe) earthquake, Interface instability, Interface slip, Modeling, Rayleigh wave.

INTRODUCTION

Earthquakes and rockbursts belong to the class of catastrophic phenomena that pose a great threat to mankind, and they have been associated with mysticism for a long time. Rockbursts are characterized by the explosive failure of underground excavations, and event magnitudes extend from the microseismic level to approximately 5 on the Richter scale, with resulting damage ranging from the ejection of small particles of rock off the face to displacement of 20,000 or more tons of rock [*Board*, 1994]. Even today, with all the computer capabilities available, there are more questions than satisfying answers. In fact, it is not at all clear how earthquakes and rockbursts are triggered and what kind of connection there exists between seismic activities and the Earth's geological structure.

Gilbert [1884] was the first geologist to notice the immediate aftereffects of the 1872 Owens Earthquake in California; as a result of his mapping the terrain he concluded that the elevation of the terrain was produced by repeated sudden ruptures along the faults. Extensive research led to the faulting theory of earthquakes proposed by H.F. Reid [see e.g. *Aki and Richards*, 1980; *Scheidegger*, 1982; *Scholz*, 1990; *Bolt*, 1993].

Seismological observations made possible by the worldwide installation of a standardized seismic network have supported the idea that shallow earthquakes are caused by fault instabilities, and it is currently accepted that dynamic faulting is the origin of the majority of seismic events. Many models have been proposed to explain the triggering mechanism of dynamic faulting [see e.g. *Scheidegger*, 1982; *Mandl*, 1988].

The classical approach to understanding of earthquake rupture mechanisms started by assuming the pre-existence of a single fault (plane of weakness or interface) in a medium. Generally, the fault is assumed to be planar, and it is assumed that rupture on the fault is controlled by friction. Three different types of models have been proposed: rigid fault plane with stick-slip; stress- and strain-singularities; and shear fracture [*Scheidegger*, 1982].

Another approach to dynamic rupture on a fault concerns vibrations normal to the fault plane. The most familiar interface waves involving separation of interface surface are Schallamach waves that occur when two media of large differences in rigidity slide past one another [*Schallamach*, 1971]. *Comninou and Dundurs* [1977, 1978a,b] showed mathematically that a dynamic wave involving separation can stably propagate along an interface when two elastic media are compressed and simultaneously sheared. However, the validity of their mathematical solution was questioned by *Freund* [1978] from an energy point of view, and the solution has mostly been ignored [*Anooshehpoor and Brune*, 1994].

From the results obtained by frictional tests in the laboratory, *Brune et al.* [*Brune et al.*, 1993; *Anooshehpoor and Brune*, 1994; *Brune*, 1996] propose that dynamic rupture on a geological fault can be triggered by interface waves with separational sections propagating along the fault. The idea is that ripples propagate along the fault and that slip occurs while the compressive stress is reduced [*Mora and Place*, 1994]. It is suggested that the excitation of Rayleigh waves on a rupture surface can lead to pulses of separation. However, this mechanism has not been confirmed in a conclusive manner [*Turcotte*, 1997].

In the present study, the basic mechanisms of dynamic fault (interface) instability caused by a Rayleigh (R-) pulse is investigated [*Rossmanith and Uenishi*, 1997; *Uenishi*, 1997; *Uenishi et al.*, 1997a,b, 1998]. The main goals are as follows:

1. To visualize and explain qualitatively the complex dynamic pulse-induced fault instability phenomena;
2. To evaluate quantitatively the pulse energy partition associated with the dynamic interaction process; and
3. To apply the experimental and numerical models to real problems of earthquakes.

First, the fundamental characteristics of an R-pulse are summarized in terms of stress field and particle motion. Second, the results of 2D laboratory model experiments utilizing dynamic photoelasticity in conjunction with high-speed cinematography are presented. It is shown that an R-pulse can trigger instability of a partially contacting interface between similar materials and that a static shear pre-stress has an influence on the initiation of interface instability. Third, the problem is numerically simulated using the finite-difference simulator SWIFD [*Rossmanith and Uenishi*, 1995, 1996], and the dynamic interaction process is quantitatively assessed. The effect of acoustic impedance mismatch of the two contacting materials on the dynamic interaction process is discussed. Finally, the results obtained by the model investigation are applied to explain the possible mechanism of the damage concentration caused by the 1995 Hyogo-ken Nanbu (Kobe), Japan, earthquake.

In the following sections, snapshots of isochromatic fringe patterns (contours of maximum in-plane shear stress) are shown to discuss the dynamic wave-pulse interaction process, because only dynamic isochromatic fringe patterns allow clear identification of the various types of stress waves in a direct way, which makes the isochromatic visualization superior to displacement and stress presentations [*Kuske and Robertson*, 1974; *Dally and Riley*, 1978; *Kobayashi*, 1993; *Rossmanith et al.*, 1997].

CHARACTERISTICS OF A RAYLEIGH PULSE

In a linear homogeneous elastic material, an R-pulse propagates in a non-dispersive fashion at smaller speed than the relevant shear (S-) wave, carrying the energy concentrated in a shallow layer adjacent to the surface with low geometrical spreading [*Rayleigh*, 1885; *Lamb*, 1904]. The stress and displacement field associated with a plane R-pulse of arbitrary shape can be analytically represented in terms of one complex potential [*Cardenas-Garcia*, 1983]. For the case of a concentrated line load on the boundary of a half-space, it is possible to determine the complex potential explicitly from the known result that the surface stress distribution due to the R-pulse is proportional to the rate of loading $dp(t)/dt$ [*Dally and Thau*, 1967]. Knowing the stress field from the complex potential, one can draw isochromatic fringe patterns pertaining to an R-pulse. A typical theoretically predicted isochromatic fringe pattern is shown in Figure 1(1) where the R-pulse, produced by a concentrated line load as a result of a detonating line charge, propagates from left to right along the free surface of the half-space [*Uenishi*, 1997]. The material properties of the half-space are listed in Table 1, and the loading function of the detonating line charge $p(t)$ is given as [*Cardenas-Garcia*, 1983]:

$$p(t) = A\sum_{n=1}^{4} B_n (t - t_n)^2 H(t - t_n)\,, \tag{1}$$

where A is the amplitude of the loading function, and $H(t)$ is Heaviside unit step function. This loading function is composed of three parabolic arc sections over the time period from $t = t_1$ (= 0) to t_4, and

$$\begin{cases} B_1 = \dfrac{1}{t_0 t_2}, \\ B_2 = -\dfrac{1}{t_2 (t_0 - t_2)}, \\ B_3 = \dfrac{t_4 - t_0}{t_0 (t_0 - t_2)(t_4 - t_3)}, \\ B_4 = -\dfrac{t_3 - t_0}{t_0 (t_0 - t_2)(t_4 - t_3)}. \end{cases} \tag{2}$$

The time t_0 when the loading function $p(t)$ reaches the maximum value A is given by [*Cardenas-Garcia*, 1983]:

$$t_0 = \frac{t_3 t_4}{t_3 + t_4 - t_2}\,, \tag{3}$$

and in this example, it is assumed for simplicity that $t_0 = 2t_2$, $t_3 = 3t_2$, and $t_4 = 4t_2$ (t_2 = 17.5μs).

As indicated by the high fringe density in Figure 1(1), the disturbance is largely confined to a thin layer adjacent to the free surface. The particle movement associated with the same R-pulse is shown in Figure 1(2) where one recognizes the push and pull normal particle movement on the free surface which becomes important in contact problems. It is interesting to note in Figure 1(2) that at depth the horizontal (parallel to the free surface) movement of particles is relatively small and vertical (into the depth) movement is dominant. Whereas in a harmonic Rayleigh wave the particles undergo closed-loop movements, this is not the case for a Rayleigh pulse where the particles may be left displaced, not forming a closed loop. This is similar to the effect of a longitudinal pulse as compared with a longitudinal harmonic wave.

Experimental Investigations

Experimental set-up

Dynamic photoelasticity in conjunction with high-speed cinematography was used to analyze the interaction between an R-pulse and a statically pre-loaded, non-welded partially contacting interface. The experimental model is schematically shown in Figure 2. The model consists of two plates of Araldite B (transparent, birefringent, isotropic, and homogeneous material) that are in contact. The experimentally obtained material properties of Araldite B are listed in Table 1. The upper surface of the plate 2 (lower plate) is given a very blunt double-wedge cut such that only the central section of the surface would initially be in contact with the upper plate (plate 1). The dimensions of the plates are selected so as to prevent reflected waves from impinging upon the region of contact and altering the results. The whole model does *not* represent the real fault segments; only central section that will be observed in the next sections models a real fault segment. The other sections are used for the purposes of wave generation and prevention of unnecessary wave reflection, and the wedge-type gap introduces a contact singularity that is utilized for contact trace purposes. They have very little bearing on the phenomenon to be investigated. Three geometrically different contact configurations (one long contact; two short contacts; and three short contacts) are investigated (Figure 3). The contact region is not glued (non-welded) and during the interaction process, the contact could diminish or be increased depending on the relative position of the R-pulse with respect to the contact region. The two plates are statically pre-loaded in compression and in shear. The static shear stress is either zero (Exp. #1), positive (Exp. #2), or reverse (Exps #3 to #5) (see Figure 3). In all experiments, *vertical* normal stress of 0.2MPa acts at the center of the contact region, which is in the linear domain of Araldite B.

The dynamic disturbance was generated in plate 1 by detonating a small amount of explosive (240mg of PbN_6) on the lower surface of plate 1 at a distance 300mm from the center of the contact region. The measured length and *maximum horizontal* normal stress of the incident R-pulse are 75mm and 7MPa, respectively (the *vertical* normal stress on the free surface is *0Pa*). For scale reasons, a grid with 25mm spacing was drawn on the side of plate 1 facing the camera.

Photoelasticity experiments utilize polarized monochromatic light, which is transmitted through the model. By using a conventional polariscope made from sheets of circularly polarizing material, optical interference occurs due to stress-induced birefringence in the model. This optical interference produces a series of light and dark bands that are termed *isochromatic fringe pattern*. The relation between the stresses in the model and the order of the fringe in the associated interference pattern is given by the stress optic law [*Dally and Riley*, 1978]:

$$2\,\tau_{max} = |\sigma_1 - \sigma_2| = f_\sigma\, N / h\,, \tag{4}$$

where τ_{max} is the maximum in-plane shear stress, σ_1 and σ_2 are the in-plane principal stresses, N is the fringe order, f_σ is the material fringe value, and h is the model thickness. This law, for two-dimensional materials, indicates that the maximum in-plane shear stress τ_{max} can be established by means of calibration. This can be done using a plane polariscope [*Dally and Riley*, 1978].

A Cranz-Schardin-type multiple-spark gap camera was used to record the dynamic fringe patterns. The multiple-spark gap camera was originally developed by *Cranz and Schardin* [1929]. For dynamic photoelastic analyses, this camera was first used in England by *Christie* [1955], and later in the United States by *Wells and Post* [1957]. In the mid-1960s, the camera was employed in a number of applications of dynamic photoelasticity [e.g. *Dally and Thau*, 1967; *Thau and Dally*, 1969], and subsequently, this camera has been effectively used in many laboratories [see e.g. *Rossmanith and Knasmillner*, 1989, 1990].

The camera was triggered by detonation of a micro-explosive, and the exposure of the first negative occurred after a selected delay period. Twenty-four frames were recorded at discrete times during the dynamic event at a framing rate of approximately 120,000 frames per second. A short exposure time of 200ns was necessary to record sharp photographic images of moving fringe patterns.

Results

In the following sections, the results obtained from the experiments are presented and discussed.

Experiment #1: compression with no shear; one long contact

In this experiment, the interaction of an R-pulse with a non-welded interface, loaded under static compression only, is investigated. Figure 4 shows a sequence of three isochromatic fringe patterns of the dynamic wave interaction process. The R-pulse propagates in the upper plate 1 from left to right and interacts with the contact region. The time scale t indicates the time elapsed from the instance of maximum stress amplification at the left-hand side (LHS) of the contact region.

Figure 4(1) pertains to the event where the incident R-pulse impinges upon the LHS of the contact region. It is clearly seen that the strength of the stress singularity, expressed by the fringe order about the LHS, is larger than that about the right-hand side (RHS), where, in this phase, the dynamic effect is still negligible. This stress amplification about the LHS is due to the particle motion on the free surface [Figure 1(2)] where the leading part of the incident R-pulse induces a back- and downward movement of the particles [Figure 4(1)]. The surface particles that are already in contact jointly move towards the lower plate 2, and thus increase the stresses about the LHS.

Whereas the first part of the retrograde motions in the incident R-pulse causes the stress amplification about the LHS, the trailing part of the R-pulse induces back- and upwardly oriented movement [Figure 1(2)], which may lead to a stress reduction with possible cancellation because the particles are now receding and open the interface. In fact, in Figure 4(2), the structure of the wave interaction patterns changes considerably. The fringe pattern about the LHS diffraction edge shows very small stress singularity.

Theoretically, the R-pulse does not exist in the contact region and there must be other kinds of generalized interface wave disturbances that carry the energy across and along the contact region. As the incident (generalized) R-pulse approaches the RHS of the contact region (seen in Figure 4(3)), partial wave energy transmission occurs across the interface into the lower plate 2. Due to the separational movements of surface particles in the trailing part of the R-pulse, the corresponding fringes in the lower plate 2 are missing (interface separation).

In summary, the retrograde motion, especially the down- and upward movement of the particles in the incident R-pulse, plays an important role in the pulse-induced interface separation (instability), as shown in Figure 5.

Experiments #2 and #3: influence of the static shear pre-loading

In the second series of experiments, a shear stress is superimposed onto the static compressive load. The shear/normal stress ratio at the center of the contact region is 0.3, and this level of shear stress is set such that the contact region is at the limiting state; that is, one still has stick contact conditions where slip will be induced at the slightest increase of the shear stress (increase in the same direction). This means, if we assume that the (cohesionless) Mohr-Coulomb condition prevails along the contact surface, the coefficient of friction is 0.3. The static shear load has been in either the positive [Exp. #2 in Figure 3(2)] or the reverse [Exp. #3 in Figure 3(3)] direction. The influence of the direction of the static shear stress is clearly seen by comparing the experimentally obtained dynamic isochromatic fringe patterns in Figure 6. In both cases, the basic wave interaction process is the same as in Experiment #1. However, the following differences can be identified:

1. The static shear stress induces an inclination of the fringes associated with the static contact stress singularity at the edges of the contact region [Figs.6(1), (3)].

2. Under static positive shear stress, the impinging R-pulse causes a relatively weak stress amplification about the LHS diffraction edge [Figure 6(1)]. This weakened amplification with less energy transmitted across the interface [Figure 6(2)] indicates that interface slip has been initiated at an earlier stage during the wave interaction process. As the shear traction level is already at the critical limit, any additional shear exerted due to particle movement within the R-pulse will trigger local slip within the contact area. When the incident R-pulse approaches the contact region and imparts a particle movement into the opposite direction of travel of the R-pulse, the positive shear stress along the contact region is increased, and slip will occur.

3. Static reverse shear stress causes larger stress amplification upon incidence of the R-pulse about the LHS diffraction edge [compare Figure 6(3) with Figure 6(1)]. This large stress intensification can be explained by considering the direction of static shear stress and the retrograde movement of particles in the R-pulse: as they act in opposite directions, immediate local slip is suppressed, and therefore, more energy can be transmitted across the contacting zone. However, when the incident R-pulse is diffracted

at the entrant edge and a complicated state of stress is generated in the volume adjacent to the contact region, as shown in Figure 6(4), no energy from the trailing part of the incident R-pulse is transmitted across the contact into the lower plate. This suggests that slip can only be initiated if the incident R-pulse is very strong, in fact, strong enough to over-compensate the reverse shear pre-stress. Interface slip may thus be inhibited and delayed, and more energy is transferred into the lower plate across the welded interface [Figure 6(4)].

Experiments #4 and #5: influence of the number of contacts

In order to study the influence of number of contacts on R-pulse scattering, a double [Exp. #4 in Figure 3(4)] and triple [Exp. #5 in Figure 3(5)] contact systems are investigated. Smaller contact lengths are chosen.

In Figure 7, isochromatic fringe patterns pertaining to two particular phases of the interaction process allow a comparison between similar dynamic situations occurring in the double [Figures 7(1) and (2)] and triple [Figures 7(3) and (4)] contact experiments. The phases shown pertain to the stages where the maximum stress amplification at the LHS edge of the first contact can be observed [Figures 7(1) and (3)], and where the transmitted R-pulse approaches the last contact section [Figures 7(2) and (4)].

The overall characteristic features of the dynamic interaction patterns, that is, stress amplification and reduction due to the R-pulse, basically appear to be similar in both experiments. However, the amplitude of the transmitted R-pulse in the upper plate shown in Figure 7(4) (i.e. after passing through two contacts) is smaller than that in Figure 7(2) (i.e. after the interaction with one contact). This indicates that each individual interaction reduces the energy of the incident/transmitted R-pulse by generating reflected R-pulses and bulk waves in the upper and lower plates.

NUMERICAL SIMULATIONS

The same dynamic pulse interaction problem is numerically investigated by using the finite-difference wave propagation simulator SWIFD (**S**olids·**W**ave·**I**mpact·**F**racture·**D**amage) [*Rossmanith and Uenishi*, 1995, 1996]. The material properties used in the numerical calculations are listed in Table 1. Here, the values are selected so that the numerical wave velocities (under pure linear elastic conditions) are comparable to the real values observed in the experiments (not perfectly linear elastic in the strict sense). For the contact problem, conditions of plane stress are assumed to prevail. The grid spacing Δx is 6.1mm, and the time step Δt is set at 1.5μs according to the Courant-Friedrichs-Lewy (CFL) condition for the stability of calculation: $\Delta t = \Delta x/(2V_P)$, where V_P is longitudinal wave speed of the material. Stress waves (including the R-pulse) are generated in the upper material by a blast source located on the surface at the point 300mm from the center of the contact region. The dynamic blast loading $p(t)$ is prescribed in the form:

$$p(t) = A\,(t / t_o)\,\exp(1 - t/t_o), \tag{5}$$

where A and t_o are parameters that characterize the amplitude and duration of the loading pulse, respectively, and can be selected to render an R-pulse with the desired maximum horizontal normal stress and length (7MPa and 75mm in this study). In addition, the R-pulse is assumed to interact with a contact region characterized by a (cohesionless) Mohr-Coulomb friction criterion with the coefficient of friction μ equal to 0.3. (This value is obtained from the experiments.) The interface is pre-stressed, and the tensile strength of the interface is set at a very low level (1kPa). The interface contact conditions are incorporated in the numerical simulation as follows [*Rossmantih and Uenishi*, 1995, 1996]:

- Initially, the interface sticks (i.e. is welded) in its normal and tangential directions. At each time step, the stresses at all nodes on the interface are calculated. If at a node the tensile stress normal to the interface exceeds the tensile strength of the interface, all degrees of freedom in the normal and the tangential directions are disconnected at that particular node (interface opening).
- If at a node i the shear stress τ_i satisfies under compression the condition (see e.g. *Mandl*, 1988):

  $$|\tau_i| \geq |\mu\,\sigma_i + T_o|, \tag{6}$$

  where μ is the coefficient of friction, σ_i is the compressive stress normal to the interface, and T_o is the cohesion parameter, only the degrees of freedom in the tangential direction are disconnected at that particular node, and the node obeys the Mohr-Coulomb condition (interface slip):

  $$|\tau_i| = |\mu\,\sigma_i + T_o|. \tag{7}$$

In this study, cohesion parameter T_o is set at 0 because it is practically very small, and by neglecting it, the calculation becomes simpler.

Pulse interaction process

Figure 8(1) shows the distribution of the normal stress acting perpendicularly to the contact region for the statically compressed, no shear, one long contact (54.9mm) case that corresponds to Experiment #1. In Figure 8(1), the coordinate axes represent the position along the initial contacting region, time from the beginning of R-pulse interaction, and the normal vertical stress. This Lagrangian-type graphical representation has been selected for improved clarity and increased information about the dynamic interaction process. The 0mm and 54.9mm positions in Figure 8(1) correspond to the LHS (incidence) and RHS (exit) edges of the contact region. The R-pulse (identified by the hump in the 3D surface) impinges on the contact region on the lower LHS and travels to the upper RHS. The maximum stress amplification at the LHS of the contact region at time $t = 0$ is clearly shown. The decay of the amplitude of the R-pulse in Figure 8(1) suggests that, initially, the tensile part of the incident R-pulse is large enough to open the interface (tensile cut-off), but when propagating along the interface, the pulse amplitude decays, and the interface opening is no longer possible at a later stage.

Figure 8(2) shows the slip distributions along the initial contacting region for the same problem (compression, no shear, and one long contact). In the figure, the coordinate axes represent the position along the initial contact region, the time elapsed with regard to the instance of maximum stress amplification at the LHS contact edge, and slip. Slip is defined by the difference of horizontal (tangential) displacements on the upper (1) and lower (2) surfaces of the interface, $u_1 - u_2$. It is shown that slip is initiated on the contact region on the lower LHS and travels to the upper RHS at the speed of the R-pulse. This indicates that slip initiation and propagation is controlled by the incident R-pulse.

Figure 9 allows comparison of the slip developments along the contact region under the two different static shear stress conditions: (1) positive shear and (2) reverse shear. In the diagrams, the ordinate shows the slip, or the relative shift between two materials, $u_1 - u_2$, and the abscissa indicates the position along the initial contacting region. The distributions of the slip are shown at four different time steps. Figure 9 suggests that slip initiation and transient state of slip during the interaction process are controlled by the incident R-pulse; however, the final (total) amount of slip after the dynamic interaction is governed by the static shear stress: in the case of positive shear [Figure 9(1)], the slip direction can be changed during the interaction process. These are consistent with the theoretical results by *Comninou and Dundurs* [1978a] that the slip induced by an interface pulse with a separational zone is relevant to the static shear stress, although in their analysis, the interface is infinitely long, and the existence of such pulses was questioned by *Freund* [1978].

Pulse energy partition

It is informative to evaluate the relative amount of energy transmitted across and reflected at the contact area during the interaction process. However, there are no expressions of energy parameters for the surface waves, and even in the simplest cases, they are given in a rather complicated form obtained by direct integration over a certain section of the wave structure [*Biryukov et al.*, 1995]. Therefore, in this study, R-pulse energy is evaluated by Fourier decomposition and considering each decomposed harmonic wave individually [*Uenishi*, 1997]. Results are schematically shown in Figure 10 for the statically compressed, however, not sheared, one long contact between two acoustically identical materials. It is indicated that more than 50% of the energy initially contained in the incident R-pulse has been radiated into the far-field in the form of bulk waves and only 37% of the total energy is transmitted along the free surface in the form of a new R-pulse R^t_1. Note that the energy carried by the reflected R-pulses is negligibly small compared with that contained in the transmitted R-pulses.

Table 2 shows the relative energy contained in the upper-transmitted R-pulse, R^t_1, after the interaction with one long contact between two acoustically identical materials. The results are shown for three different static shear pre-loading conditions. It is indicated that positive (reverse) static shear pre-loading does increase (decrease) the energy transmitted along the contact region in material 1, respectively. These results are consistent with the experiments [Figure 6] where less (more) energy transfer across the contact region into material 2 has been observed under positive (reverse) static shear stress, respectively.

Comparison of numerical and experimental results

In this section, validity of the numerical simulations is discussed by comparing the numerical results with the experimental ones. Comparison of numerically generated and experimentally obtained (Exp.#1) isochromatic fringe patterns shown in Figure 11 exhibits very similar pulse interaction patterns: the stress amplification [at stage (1)] and reduction [at stage (2)] at the LHS of the contact region can be seen.

The energy transmission coefficients calculated from the numerical data and experimental fringe patterns are plotted in Figure 12 under different static shear conditions [Exps #1-3], showing similar pulse energy partition patterns and the maximum difference of coefficients of 3.7% between numerics and experiments.

From the previous two comparisons, it may be concluded that the finite-difference code SWIFD can well simulate the rather complex dynamic interaction process [*Uenishi*, 1997].

Influence of the acoustic impedance mismatch

During the course of numerical investigations, the influence of acoustic impedance ratio $(\rho V_P)_2/(\rho V_P)_1$ was also studied. Here, ρ is the mass density, V_P is the longitudinal (P-) wave speed, and the subscripts 1 and 2 correspond to the upper and lower material, respectively. The acoustic impedance ratio of the two contacting materials plays a crucial role in wave transmission and reflection at the interface [see e.g. *Rinehart*, 1975]. The investigation was performed for one long contact under static compression only.

Figure 13 shows the numerically generated snapshots of isochromatic fringe patterns taken at the same timing, 60μs after the maximum stress amplification at the LHS edge of the contact region. Figure 13(1) pertains to the case where the incident R-pulse speed lies between the shear (S-) and P-wave speeds of the lower material, $(V_S)_2<(V_R)_1<(V_P)_2$ [$(V_R)_1/(V_S)_2=1.379$; $(V_R)_1/(V_P)_2=0.796$]. Since the slip pulse propagates at the Rayleigh wave speed of the acoustically harder material 1, $(V_R)_1$, the pulse energy is transferred along the contact region at transonic speed with respect to the acoustically softer material 2. A shear-type (S-) Mach (head) wave is generated that propagates from the contact region into material 2.

If the lower material is sufficiently soft, $(V_S)_2<(V_P)_2<(V_R)_1$ [$(V_R)_1/(V_S)_2=2.308$; $(V_R)_1/(V_P)_2=1.332$ in Figure 13(2)], the energy is transmitted across the contact region supersonically into the softer material 2 and both longitudinal- (P-) and shear-type (S-) Mach waves are generated, and the disturbance in the lower material 2 is largely confined to the region behind the P-Mach wave front.

Both cases shown in Figure 13 indicate that interface rupture pulse can propagate at the speed of Rayleigh wave of the acoustically harder material 1.

DISCUSSION

Fracture along an interface versus fracture in a monolithic medium

Figure 8 has revealed that the interface slip initiation is controlled by the incident R-pulse and that the slip pulse propagates at the incident R-pulse speed.

The relation between the Rayleigh wave (pulse) speed V_R and the relevant shear wave speed V_S is approximately given by [*Viktorov*, 1962]:

$$\frac{V_R}{V_S} \approx \frac{0.87 + 1.12\nu^*}{1+\nu^*}, \tag{8}$$

where ν^* is generalized Poisson's ratio [$\nu^* = \nu$ (Poisson's ratio) for plane strain, and $\nu^* = \nu/(1+\nu)$ for plane stress conditions]. For example, for rock with $\nu^* = 0.25$, $V_R/V_S = 0.92$, which indicates that a slip pulse can propagate at a speed of about 90% of the shear wave speed of the material. This relatively high rupture propagation speed seems contradictory to the previous experimental results.

In the past, rupture associated with earthquakes was studied within the framework of dynamic fracture mechanics (crack propagation) in a monolithic material. *Broberg* [1960] showed that the speed of a remotely loaded traction-free crack in a homogeneous material cannot exceed the Rayleigh wave speed V_R of that material and that an infinite amount of energy would have to be fed into the crack tip in order to maintain further crack extension at speed V_R if the stress intensity factor was non-zero [see e.g. *Freund*, 1990]. This requirement obviously makes it energetically impossible for a crack in a homogeneous solid to become or exceed the material's Rayleigh wave speed [*Lambros and Rosakis*, 1995a].

Recently, dynamic interface fracture mechanics has attracted the attention of researchers in fracture mechanics. Due to the intrinsic difficulties associated with this problem, however, only a few theoretical studies have been performed, and there is a strong disagreement as to the theoretically predicted value of the terminal velocity for propagating interface cracks. *Willis*

[1973] suggested that the terminal speed of an interface crack should be slightly larger than the Rayleigh wave speed of the more compliant of the two constituents, while *Atkinson* [1977] claimed that the terminal speed should be the lower Rayleigh wave speed of the two materials [*Lambros and Rosakis*, 1995a]. *Weertman* [1980] studied an edge dislocation moving along a material interface at a constant velocity and suggested that a dynamic reduction in compressive normal traction may allow a slip pulse to propagate in a self-sustaining manner near the shear wave speed of the softer material along an interface governed by a constant coefficient of friction [*Andrews and Ben-Zion*, 1997].

More recently, using the experimental technique of shearography, Lambros and Rosakis [1995a,b] and Liu *et al.*, [1995] have investigated dynamic interfacial delamination in dissimilar media. They showed experimentally as well as analytically that, under certain loading conditions, the speed of a propagating interface crack in a bimaterial system may exceed the Rayleigh and the shear wave speeds of the softer material [*Lambros and Rosakis*, 1995a,b; *Liu et al.*, 1995]. This result, consistent with the high propagation speed of a rupture pulse observed in this study, indicates the fundamental difference between interface fracture and fracture in a monolithic medium.

Interface pulse with a separational zone

Interface separation (fault rupture) induced by a pulse has been clearly seen in the experimentally obtained snapshot [Figure 4(3)]. In this section, seismological meaning and importance of such a slip pulse is discussed.

In the classical analysis of earthquake rupture mechanisms, rupture will be initiated at one point on the fault and will spread across the fault surface. Slip occurs across the entire fault zone until rupture propagation is arrested. However, *Heaton* [1990] showed, based on seismic inversions, that local rise times for fault slip are much shorter than would be the case for the classical model. As a model for the short rise time observed, he suggested that self-healing pulses of slip occur in earthquake ruptures [*Turcotte*, 1997]. *Day* [1991] indicated numerically that, along a statically pre-stressed interface between similar materials, the wave of separation decays rapidly rather than propagates in a self-sustaining manner. However, *Mora and Place* [1994] showed, again numerically, that self-healing pulses can be sustained if interface surface roughness is present. *Andrews and Ben-Zion* [1997] conducted two-dimensional numerical simulations of dynamic rupture along a planar material interface governed by simple friction. Their results showed self-sustaining propagation of slip pulse and spontaneous break up of the propagating pulse to a number of smaller pulses. However, the details and the controlling parameters of the interface slip pulse propagation are not yet known; therefore, further investigation is needed.

If an interface pulse with a separational zone can propagate at depth in the Earth where very high compressive stress is expected, such a pulse (as suggested by Brune *et al.*, [1993], Anooshehpoor and Brune [1994], Brune [1996], and Andrews and Ben-Zion [1997]) may be a solution to the long-standing paradoxes associated with earthquakes: the origin of short rise times in earthquake slip [*Heaton*, 1990]; dynamic contributions to spatio-temporal slip complexities [see e.g. *Rice*, 1993; *Ben-Zion and Rice*, 1995, 1997; *Cochard and Madariaga*, 1996]; the anomalous P-wave radiation [see e.g. *Haskell*, 1964; *Molnar et al.*, 1973; *Anooshehpoor and Brune*, 1994]; the heat flow paradox [see e.g. *Brune et al.*, 1969; *Henyey and Wasserburg*, 1971; *Lachenbruch and Sass*, 1988, 1992; *Williams et al.*, 1988]; and the low static shear stress levels on geological faults [see e.g. *Mount and Suppe*, 1987; *Zoback et al.*, 1987, 1988; *Jones*, 1988; *Oppenheimer et al.*, 1988; *Turcotte*, 1991, 1997; *Lachenbruch and Sass*, 1992; *Zoback and Healy*, 1992].

Influence of fault topography

In reality, the crustal rock adjacent to geological faults is fragmented by secondary faults over a wide range of scales. In modeling earthquakes, one consequence of this complexity is the introduction of the concept of asperities. The regions of very high slip, or asperities, are considered to be important in earthquake hazard analysis because the failure of the asperities radiates most of the high-frequency seismic energy into the far-field. The geometrical explanation for asperities reflects the fact that real faults are not perfectly planar, and their topography shows roughness on all scales, containing jogs or steps [*Scholz*, 1990; *Lay and Wallace*, 1995; *Turcotte*, 1997].

This study has shown that a relatively large amount of energy is radiated in the form of bulk waves from a contact region into the far-field. Interface slip is found only inside the initial contacting regions. These observations suggest that (when scaled up) the contact regions in the model can be regarded as asperities on a geological fault. Therefore, the energy partition patterns obtained from the laboratory and numerical models may be of practical importance in evaluating the influence of asperities. A practical example is given in the next section.

Case example – the 1995 Hyogo-ken Nanbu (Kobe), Japan, earthquake

On 17 January 1995, at 5:46 a.m. local time, an earthquake of moment magnitude 6.9 struck the region of Kobe and Osaka (Hanshin region) in west-central Japan. This region is one of the most populated and industrialized areas, with a population of about 10 million. Seismic inversion [*Wald*, 1995, 1996] suggests that the rupture started at a shallow depth on a fault system running from Awaji Island through the city of Kobe and propagated bilaterally: along the Suma and Suwayama faults toward the city of Kobe and along the Nojima fault [Figure 14(1)]. Strong ground motion lasted for some 20 seconds and caused considerable damage within a radius of 100km from the epicenter, but most severely affected were Kobe and its neighboring cities [*EQE International*, 1995].

One of the mystifying phenomena observed in Kobe [*Kawase*, 1996a,b; *Suzuki et al.*, 1996] is the emergence of the strip of the most severely damaged zone [the Japan Meteorological Agency Intensity 7 zone marked in dark gray in Figure 14(1)]. This strip (the damage belt), approximately 20km long, is located close, but not parallel, to the Suma/Suwayama faults. Damage due to liquefaction was hardly observed inside this area, and it is suggested that the damage was caused directly by the seismic waves (e.g. the damage due to the seismic wave amplification in the deep basin structure (the "edge effect") [*Kawase*, 1996b; *Pitarka et al.*, 1998]).

As the Suma and Suwayama faults dip steeply, nearly 90°, and a near-source, SH directivity pulse from strike-slip faulting was recorded in the city of Kobe [*Nakamura*, 1995; *Toki et al.*, 1995], a two-dimensional model, which includes a plane perpendicular to the fault plane, is considered appropriate for an approximate first-order analysis of the rupture mechanisms of the Hyogo-ken Nanbu earthquake.

A region of relatively large slip (asperity) was found beneath the LHS [in Figure 14(1)] of the strip [*Wald*, 1995, 1996]. A concentrated shear disturbance arrived, and the resulting large (particle) velocity response was recorded in central Kobe [*Wald*, 1996]. This suggests that the rupture-induced shear wave was of a Mach (head) wave type. Note here that Mach waves generated at fault zones have also been theoretically predicted for planar material interfaces [e.g. *Ben-Zion and Aki*, 1990], and they have been observed along several sections of the San Andreas fault [*McNally and McEvilly*, 1977; *Ben-Zion and Malin*, 1991; *Andrews and Ben-Zion*, 1997], along small segments in the Mojave, eastern California, shear zone [*Hough et al.*, 1994; *Andrews and Ben-Zion*, 1997].

As discussed earlier, an asperity on a fault corresponds to a contact region in the model. In Figure 13(1), where an interface is located between dissimilar materials [$(V_S)_2<(V_R)_1<(V_P)_2$], an S-Mach wave is observed in the numerical simulation. In the model, material 1 corresponds to the acoustically harder region in the foothills of the Rokko Mountains, where soils are very shallow or rock outcroppings are found. There the damage tended to be relatively minor. Material 2 fits the acoustically softer region (where primarily soft alluvial soils prevail), which includes the damage belt.

During the course of dynamic interaction, each particle in the materials will experience a history of velocity and acceleration. The maximum values of these quantities are of practical importance, and, hence, the peak particle velocity (PPV) and the peak particle acceleration (PPA) have been selected as the design parameters in many applications such as blasting in mines and quarries, and in engineering seismology.

Figure 14 shows the distributions of PPV [Figure 14(2)] and PPA [Figure 14(3)] obtained by the numerical simulation [$(V_S)_2<(V_R)_1<(V_P)_2$, where $(V_R)_1/(V_S)_2$=1.379; $(V_R)_1/(V_P)_2$=0.796]. It is interesting to note that the region of high PPV (or PPA) is located in a narrow band, similar to the shape of the damage belt in Kobe [see RHS figure of Figure 14(1)]. The angle between the interface (fault) and the region of high PPV (PPA) in this example is controlled by the propagation direction of the S-Mach wave generated during the interaction process [Figure 13(1)]. This result indicates that a simple two-dimensional model may be able to provide the information about the earthquake rupture and the ensuing dynamic wave phenomena, although a more sophisticated study would have to be based on a three-dimensional analysis that includes local geological as well as topographical effects on the real fault rupture process.

CONCLUSIONS

The purpose of this study was to obtain an improved understanding of the pulse-induced instability of a fault between similar and dissimilar materials. The experimental and numerical model investigations have given a clear insight into the basic mechanisms of the Rayleigh (R-) pulse-induced instability of a statically pre-stressed fault: fault interface separation (instability) can be induced by an R-pulse, and the observed dynamic stress amplification and reduction at the interface are caused by the push and pull normal particle motion associated with an R-pulse. It has been shown that the influence of the direction of the static shear stress on slip initiation can be considerable: under static positive shear stress, the impinging R-pulse causes a relatively weak stress intensification with less energy transmission across the interface, indicating enhanced interface slip initiation. If the static positive shear traction level is already at the critical limit, any additional shear exerted due to particle movement within the R-pulse triggers local slip. On the other hand, static reverse shear stress causes larger stress amplification upon incidence of the R-pulse. As static shear stress and the retrograde movement of particles in the R-pulse act in opposite directions, immediate local slip is suppressed, and more energy can be transferred across the contacting zone. Slip can only be initiated if the incident R-pulse is strong enough to over-compensate the reverse shear pre-stress. Interface slip may thus be inhibited and delayed.

The SWIFD finite-difference simulator has provided quantitative information about the pulse-fault interaction process. It has been shown that: (1) A slip pulse can propagate at the Rayleigh wave speed of the acoustically harder material (about 90% of the shear wave speed of that material); (2) Under the action of static positive shear stress, fault slip direction can change during the dynamic interaction process; and (3) Pulse interaction patterns are controlled by the acoustic impedance mismatch of the contacting materials, and Mach (head) waves can be generated at and propagated from a contact region between dissimilar materials.

The relatively high rupture propagation speed observed in the model study seems contradictory to the previous experimental results, which predict that it is energetically impossible for a crack in a monolithic solid to propagate faster than the material's Rayleigh wave. Recent research in dynamic interface fracture mechanics, however, has shown experimentally as well as analytically that, under certain loading conditions, the speed of a propagating interface crack in a bimaterial system may exceed the Rayleigh and the shear wave speeds of the softer material [*Lambros and Rosakis*, 1995a,b; *Liu et al.*, 1995]. This result, consistent with the high propagation speed of a rupture pulse observed in this study, indicates the fundamental difference between interface fracture and fracture in a monolithic medium.

In modeling earthquakes, the regions of very high slip, or asperities, are considered to be important because the rupture of the asperities radiates most of the high-frequency seismic energy into the far-field. This study has shown that a relatively large amount of energy is radiated in the form of bulk waves from a contact region into the far-field. This observation suggests that the contact regions in the model, when scaled up, can be regarded as asperities on a fault. Therefore, the energy partition patterns obtained from the model study may be practically important in evaluating the influence of asperities.

As a case example, damage concentration mechanism associated with the 17 January 1995 Hyogo-ken Nanbu (Kobe), Japan, earthquake has been studied using the 2D numerical model. It has been suggested that the rupture-induced shear wave was a Mach (head) wave that propagated from a rupturing asperity (contact region) located between dissimilar materials. The numerical simulation has shown that the regions of high PPV (peak particle velocity) and PPA (peak particle acceleration) form a narrow band, which is similar to the shape of the strip of the most severely damaged zone in Kobe. It is hoped that the knowledge gained from this work will assist in obtaining a better understanding of the fault rupture mechanisms. It should also be noted that because of a vast variety of application areas of Rayleigh pulses, the basic phenomena observed in this study might be of practical importance in various other fields of engineering.

ACKNOWLEDGMENTS

This work was financially sponsored by the Austrian National Science Foundation (FWF) through Research Project Number P10326-GEO. The authors would like to thank Prof. R. Madariaga, Prof. H. Kawase, and the anonymous reviewer for their suggestions to improve this article.

REFERENCES

Aki, K., and P.G. Richards, *Quantitative Seismology*, W.H. Freeman and Company, San Francisco, 1980.

Andrews, D.J., and Y. Ben-Zion, Wrinkle-like slip pulse on a fault between different materials, *J. Geophys. Res.*, *102*, 553-571, 1997.

Anooshehpoor, A., and J.N. Brune, Frictional heat generation and seismic radiation in a foam rubber model of earthquakes, *Pure Appl. Geophys.*, *143*, 735-747, 1994.

Atkinson, C., Dynamic crack problems in dissimilar media, in *Mechanics of Fracture Vol.4*, edited by G.C. Sih, pp.213-248, Noordhoff, Leyden, Netherlands, 1977.

Ben-Zion, Y., and K. Aki, Seismic radiation from an SH line source in a laterally heterogeneous planar fault zone, *Bull. Seismol. Soc. Am.*, *80*, 971-994, 1990.

Ben-Zion, Y., and P. Malin, San Andreas fault zone head waves near Parkfield, California, *Science*, *251*, 1592-1594, 1991.

Ben-Zion, Y., and J.R. Rice, Slip patterns and earthquake populations along different classes of faults in elastic solids, *J. Geophys. Res.*, *100*, 12,959-12,983, 1995.

Ben-Zion, Y., and J.R. Rice, Dynamic simulations of slip on a smooth fault in an elastic solid, *J. Geophys. Res.*, *102*, 17,771-17,784, 1997.

Biryukov, S.V., Yu.V. Gulyaev, V.V. Krylov, V.P. Plessky, *Surface Acoustic Waves in Inhomogeneous Media*, 388pp., Springer-Verlag, Berlin, 1995.

Board, M.P., Numerical examination of mining-induced seismicity, Ph.D. Thesis, University of Minnesota, 1994.

Bolt, B.A., *Earthquakes and Geological Discovery*, 229pp., Scientific American Library, New York, 1993.

Broberg, K.B., The propagation of a Griffith crack, *Ark. Fys.*, *18*, 159-192, 1960.

Brune, J.N., Particle motions in a physical model of shallow angle thrust faulting, *Proc. Indian Acad. Sci. (Earth Planet. Sci.)*, *105*, L197-L206, 1996.

Brune, J.N., T.L. Henyey, and R.F. Roy, Heat flow, stress, and rate of slip along the San Andreas fault, California, *J. Geophys. Res.*, *74*, 3821-3827, 1969.

Brune, J.N., S. Brown, and P.A. Johnson, Rupture mechanism and interface separation in foam rubber models of earthquakes: a possible solution to the heat flow paradox and the paradox of large overthrusts, *Tectonophysics*, *218*, 59-67, 1993.

Cardenas-Garcia, J.F., On Rayleigh waves and Rayleigh wave extension of surface micro-cracks, Ph.D. Thesis, University of Maryland, College Park, 1983.

Christie, D.G., A multiple spark camera for dynamic stress analysis, *Journal of Photographic Science*, *3*, 153-159, 1955.

Cochard, A., and R. Madariaga, Complexity of seismicity due to highly rate-dependent friction, *J. Geophys. Res.*, *101*, 25,321-25,336, 1996.

Comninou, M., and J. Dundurs, Elastic interface waves involving separation, *J. Appl. Mech.*, *44*, 222-226, 1977.

Comninou, M., and J. Dundurs, Can two solids slide without slipping? *Int. J. Solids Structures*, *14*, 251-260, 1978a.

Comninou, M., and J. Dundurs, Elastic interface waves and sliding between two solids, *J. Appl. Mech.*, *45*, 325-330, 1978b.

Cranz, C., and H. Schardin, Kinematographic auf ruhendem Film und mit extremhohen Bild Frequenz, *Zeit. f. Phys.*, *56*, 147-183, 1929.

Dally, J.W., and W.F. Riley, *Experimental Stress Analysis*, 571pp., McGraw-Hill, New York, 1978.

Dally, J.W., and S.A. Thau, Observations of stress wave propagation in a half-plane with boundary loading. *Int. J. Solids Structures*, *3*, 293-308, 1967.

Day, S.M., Numerical simulation of fault propagation with interface separation (abstract), *EOS Trans. AGU 72(44)*, Fall Meet. Suppl., 486, 1991.

EQE International, *The January 17, 1995 Kobe Earthquake*, EQE International, San Francisco, 1995.

Freund, L.B., Discussion: elastic interface waves involving separation, *J. Appl. Mech.*, *45*, 226-228, 1978.

Freund, L.B., *Dynamic Fracture Mechanics*, 563pp., Cambridge University Press, Cambridge, 1990.

Gilbert, G.K., A theory of earthquakes of the great basin with a practical application, *Am. J. Sci.*, *27*, 49-54, 1884.

Haskell, N., Total energy and energy spectral density of elastic wave radiation from propagating faults, *Bull. Seismol. Soc. Am.*, *54*, 1811-1841, 1964.

Heaton, T.H., Evidence for and implications of self-healing pulses of slip in earthquake rupture, *Phys. Earth Planet. Int.*, *64*, 1-20, 1990.

Henyey, T.L., and G.J. Wasserburg, Heat flow near major strike-slip faults in California, *J. Geophys. Res.*, *76*, 7924-7964, 1971.

Hough, S.E., Y. Ben-Zion, and P. Leary, Fault-zone waves observed at the southern Joshua Tree earthquake rupture zone, *Bull. Seismol. Soc. Am.*, *84*, 761-767, 1994.

Jones, L., Focal mechanisms and the state of stress on the San Andreas fault in southern California, *J. Geophys. Res.*, *93*, 8869-8892, 1988.

Kawase, H., Site effects observed during the Hyogo-Ken Nanbu earthquake of 1995 and strong motion simulation including the basin-edge effect, in *Proceedings of the Eleventh World Conference on Earthquake Engineering*, paper No.2031, Elsevier Science, Oxford, 1996a.

Kawase, H., The cause of the damage belt in Kobe: "The basin-edge effect", Constructive interference of the direct S-wave with the basin-induced diffracted / Rayleigh waves, *Seism. Res. Let.*, *67*, 25-35, 1996b.

Kobayashi, A.S., *Handbook on Experimental Mechanics*, 1074pp., SEM, Bethel CT, USA, 1993.

Kuske, A., and G. Robertson, *Photoelastic Stress Analysis*, 519pp., John Wiley & Sons, New York, 1974.

Lachenbruch, A.H., and J.H. Sass, The stress heat-flow paradox and thermal results from Cajon Pass, *Geophys. Res. Let.*, *15*, 981-984, 1988.

Lachenbruch, A.H., and J.H. Sass, Heat flow from Cajon Pass, fault strength, and tectonic implications, *J. Geophys. Res.*, *97*, 4995-5015, 1992.

Lamb, H., On the propagation of tremors over the surface of an elastic solid, *Phil. Trans. Roy. Soc. London*, *A203*, 1-42, 1904.

Lambros, J., and A.J. Rosakis, Shear dominated transonic interfacial crack growth in a bimaterial – I. Experimental observations, *J. Mech. Phys. Solids*, *43*, 169-188, 1995a.

Lambros, J., and A.J. Rosakis, Development of a dynamic decohesion criterion for subsonic fracture of the interface between two dissimilar materials, *Proc. R. Soc. Lond.*, *A451*, 711-736, 1995b.

Lay, T., and T.C. Wallace, *Modern Global Seismology*, 517pp., Academic Press, San Diego, 1995.

Liu, C., Y. Huang, and A.J. Rosakis, Shear dominated transonic interfacial crack growth in a bimaterial – II. Asymptotic fields and favorable velocity regimes, *J. Mech. Phys. Solids*, *43*, 189-206, 1995.

McNally, K.C., and T.V. McEvilly, Velocity contrast across the San Andreas fault in central California: small-scale variations from P-wave nodal plane distortion, *Bull. Seismol. Soc. Am.*, *67*, 1565-1576, 1977.

Mandl, G., *Mechanics of Tectonic Faulting: Models and Basic Concepts*, 407pp., Elsevier, Amsterdam, 1988.

Molnar, P., B.E. Tucker, and J.N. Brune, Corner frequencies of P and S waves and models of earthquake sources, *Bull. Seismol. Soc. Am.*, *63*, 2091-2104, 1973.

Mora, P., and D. Place, Simulation of the frictional stick-slip instability, *Pure Appl. Geophys.*, *143*, 61-87, 1994.

Mount, V.S., and J. Suppe, State of stress near the San Andreas fault: implications for wrench tectonics, *Geology*, *15*, 1143-1146, 1987.

Nakamura, Y., Waveform and its analysis of the 1995 Hyogo-Ken-Nanbu earthquake, *JR Earthquake Information*, *23c*, Railway Technical Research Institute, 1995.

Oppenheimer, D., P. Reasenberg, and R. Simpson, Fault plane solutions for the 1984 Morgan Hill, California, earthquake sequence: evidence for the state of stress on the Calaveras fault, *J. Geophys. Res.*, *93*, 9007-9026, 1988.

Pitarka, A., K. Irikura, T. Iwata, and H. Sekiguchi, Three-dimensional simulation of the near-fault ground motion for the 1995 Hyogo-ken Nanbu (Kobe), Japan, earthquake, *Bull. Seismol. Soc. Am.*, *88*, 428-440, 1998.

Rayleigh, J.W.S., On waves propagated along the plane surface of an elastic solid, *The Proceedings of the London Mathematical Society*, *17*, 4-11, 1885.

Rice, J.R., Spatio-temporal complexity of slip on a fault, *J. Geophys. Res.*, *98*, 9885-9907, 1993.

Rinehart, J.S., *Stress Transients in Solids*, 230pp., HyperDynamics, Santa Fe, 1975.

Rossmanith, H.P., and R.E. Knasmillner, Diffraction of Rayleigh waves at surface irregularities, *Appl. Mech. Rev.*, *42*, S223-S232, 1989.

Rossmanith, H.P., and R.E. Knasmillner, The role of Rayleigh-waves in rock fragmentation, in: *The Proceedings of the Third International Symposium on Rock Fragmentation by Blasting*, pp.109-116, The Australasian Institute of Mining and Metallurgy, Parkville, Victoria, Australia, 1990.

Rossmanith, H.P., and K. Uenishi, *SWIFD User's Manual Version 1995*, 73pp., Fracture and Photo-Mechanics Laboratory, Vienna University of Technology, Vienna, 1995.

Rossmanith, H.P., and K. Uenishi, PC software assisted teaching and learning of dynamic fracture and wave propagation phenomena, in *Teaching and Education in Fracture and Fatigue*, edited by H.P. Rossmanith, pp.253-262, E & FN Spon, London, 1996.

Rossmanith, H.P., and K. Uenishi, Fault dynamics – dynamic triggering of fault slip, in *Proceedings of the International Symposium on Rock Stress*, edited by K. Sugawara and Y. Obara, pp.27-34, A.A. Balkema, Rotterdam, 1997.

Rossmanith, H.P., K. Uenishi, and N. Kouzniak, Blast wave propagation in rock mass – part I: monolithic medium, *FRAGBLAST*, **1**, 317-359.

Schallamach, A., How does rubber slide? *Wear*, *17*, 301-312, 1971.

Scheidegger, A.E., *Principles of Geodynamics (Third, Completely Revised Edition)*, 395pp., Springer-Verlag, Berlin, 1982.

Scholz, C.H., *The Mechanics of Earthquakes and Faulting*, 439pp., Cambridge University Press, New York, 1990.

Suzuki, T., M. Hakuno, and S. Igarashi, Numerical simulation on magnification of the ground motion in the irregular surface layer, in *Proceedings of the Eleventh World Conference on Earthquake Engineering*, paper No.305, Elsevier Science, Oxford, 1996.

Thau, S.A., and J.W. Dally, Subsurface characteristics of the Rayleigh wave, *Int. J. Engng Sci.*, *7*, 37-52, 1969.

Toki, K., K. Irikura, and T. Kagawa, Strong motion data recorded in the source area of the Hyogo-Ken-Nanbu earthquake, January 17, 1995, Japan, *J. Nat. Disas. Sci.*, *16*, 23-30, 1995.

Turcotte, D.L., Earthquake prediction, *Annu. Rev. Earth Planet. Sci.*, *19*, 263-281, 1991.

Turcotte, D.L., Earthquakes, fracture, complexity, in *Proceedings of the IUTAM Symposium on Nonlinear Analysis of Fracture*, edited by J.R. Willis, pp.163-175, Kluwer Academic Publishers, Dortrecht, 1997.

Uenishi, K. Rayleigh pulse – dynamic triggering of interface slip, Ph.D. Thesis, Vienna Univ. of Technol., Vienna, 1997.

Uenishi, K., H.P. Rossmanith, and R.E. Knasmillner, Interaction of Rayleigh pulse with non-uniformly contacting interfaces, in *Proceedings of the International Conference on Materials and Mechanics '97*, pp.95-100, The Japan Society of Mechanical Engineers, Tokyo, 1997a.

Uenishi, K., H.P. Rossmanith, R.E. Knasmillner, and C. Böswarth. Rayleigh pulse interaction with partially contacting dissimilar interfaces, in *Proceedings of the First International*

Conference on Damage and Failure of Interfaces, pp.305-314, A.A. Balkema, Rotterdam, 1997b.

Uenishi, K., H.P. Rossmanith, and R.E. Knasmillner. Rayleigh pulse-induced fault slip: model and application, in *Proceedings of the Third International Conference on the Mechanics of Jointed and Faulted Rock*, pp.249-254, A.A.Balkema, Rotterdam, 1998.

Viktorov, I.A., Rayleigh waves in the ultrasonic range, *Soviet Physics – Acoustics*, *8*, 118-129, 1962.

Wald, D.J., A preliminary dislocation model for the 1995 Kobe (Hyogo-Ken Nanbu), Japan, earthquake determined from strong motion and teleseismic waveforms, *Seism. Res. Let.*, *66*, 22-28, 1995.

Wald, D.J., Slip history of the 1995 Kobe, Japan, earthquake determined from strong motion, teleseismic, and geodetic data, *J. Phys. Earth*, *44*, 489-503, 1996.

Weertman, J., Unstable slippage across a fault that separates elastic media of different elastic constants, *J. Geophys. Res.*, *85*, 1455-1461, 1980.

Wells, A.A., and D. Post, The dynamic stress distribution surrounding a running crack – a photoelastic analysis. *SESA Proceedings*, *XVI*, 69-92, 1957.

Williams, P.L., S.F. McGill, K.E. Sieh, C.R. Allen, and J.N. Louie, Triggered slip along the San Andreas fault after the 8 July 1986 North Palm Springs earthquake, *Bull. Seismol. Soc. Am.*, *78*, 1112-1122, 1988.

Willis, J.R., Self-similar problems in elastodynamics, *Phil. Trans. R. Soc. Lond.*, *274*, 435-491, 1973.

Zoback, M.D., and J.H. Healy, In situ stress measurements to 3.5km depth in the Cajon Pass scientific research borehole: implications for the mechanics of crustal faulting, *J. Geophys. Res.*, *97*, 5039-5057, 1992.

Zoback, M.D., M.L. Zoback, V.S. Mount, J. Suppe, J.P. Eaton, J.H. Healy, D. Oppenheimer, P. Reasenberg, L. Jones, C.B. Raleigh, I.G. Wong, O. Scotti, and C. Wentworth, New evidence on the state of stress of the San Andreas fault system, *Science*, *238*, 1105-1111, 1987.

Zoback, M.D., L.T. Silver, T. Henyey, and W. Thatcher, The Cajon Pass scientific drilling experiment: overview of phase I, *Geophys. Res. Let.*, *15*, 933-936, 1988.

INSTITUTE OF MECHANICS, VIENNA UNIVERSITY OF TECHNOLOGY
WIEDNER HAUPTSTR. 8-10/325, A-1040 VIENNA, AUSTRIA
(K.U.*, H.P.R.)

INSTITUTE OF THEORETICAL GEODESY AND GEOPHYSICS, VIENNA UNIVERSITY OF TECHNOLOGY
GUSSHAUSSTR. 25-29, A-1040 VIENNA, AUSTRIA
(A.E.S.)

* PRESENT ADDRESS: DEPARTMENT OF ARCHITECTURE AND CIVIL ENGINEERING, KOBE UNIVERSITY
ROKKO-DAI 1-1, NADA, KOBE 657-8501 JAPAN

Table 1. The properties of the model material.

Model material	Analytical and numerical model (elastic material; plane stress)	Araldite B (experimental data)
Mass density	1260kg/m^3	1260kg/m^3
Young's modulus	4.63GPa	4.34GPa
Shear modulus	1.74GPa	1.63GPa
Poisson's ratio	0.33	0.39
Longitudinal wave speed (V_P)	2033m/s	2004m/s
Shear wave speed (V_S)	1174m/s	1156m/s
Rayleigh wave speed (V_R)	1080m/s	1105m/s
Material fringe value (f_σ)	---	10.12MPa•mm/fringe

Table 2. Relative energy in the upper-transmitted R-pulse after the interaction with one long contact.

Static shear	Reverse shear	No shear	Positive shear
Relative energy contained in R^t_1	29%	37%	41%

Figure Legends

Figure 1. A Rayleigh pulse propagating from left to right along a free surface:
(1) Isochromatic fringe patterns (contours of maximum shear stress); and
(2) Vector representation of displacements and particle movements at different depths..

Figure 2. The experimental model set-up for Rayleigh pulse interaction investigation [all lengths in millimeters].

Figure 3. Five experiments of Rayleigh pulse interaction with a partially contacting interface [all lengths in millimeters]:
(1) Compression with no shear; one long contact;
(2) Compression with positive shear; one long contact;
(3) Compression with reverse shear; one long contact;
(4) Compression with reverse shear; two short contacts; and
(5) Compression with reverse shear; three short contacts.

Figure 4. Sequence of experimentally obtained snapshots of isochromatic fringe patterns. Experiment #1: compression with no shear; one long contact.

Figure 5. Interface opening caused by a Rayleigh (R-) pulse.

Figure 6. Dynamic isochromatic fringe patterns.
(1, 2): Experiment #2: compression with positive shear; one long contact.
(3, 4): Experiment #3: compression with reverse shear; one long contact.

Figure 7. Snapshots of isochromatic fringe patterns obtained by experiments.
(1, 2): Experiment #4: compression with reverse shear; two short contacts; and
(3, 4): Experiment #5: compression with reverse shear; three short contacts.

Figure 8. Quantitative information about the pulse interaction process.
(1) Vertical normal stress acting on the contact region; and
(2) Slip development along the contact region.

Figure 9. Development of slip along the initially contacting region.
(1) Compression with positive shear; and (2) Compression with reverse shear.

Figure 10. Partition of the energy contained in the incident R-pulse for the case where the two contacting materials are mechanically identical.

Figure 11. Comparison of snapshots of isochromatic fringe patterns obtained by:
Left column: numerical simulation; and right column: Experiment #1.

Figure 12. Comparison of pulse energy transmission coefficients obtained by the numerical simulations and the experiments under different static shear conditions.

Figure 13. Snapshots of isochromatic fringe patterns under two different combinations of contacting materials. (1) $(V_S)_2 < (V_R)_1 < (V_P)_2$; and (2) $(V_S)_2 < (V_P)_2 < (V_R)_1$.

Figure 14. Comparison of the Hyogo-ken Nanbu (Kobe) earthquake and the numerical simulation [for the case $(V_S)_2 < (V_R)_1 < (V_P)_2$]. (1) the Japan Meteorological Agency Intensity 7 (the most severely damaged) zone (dark gray region) associated with the Kobe earthquake; and contours of (2) high PPV (peak particle velocity) and (3) high PPA (peak particle acceleration) obtained by the numerical simulation.

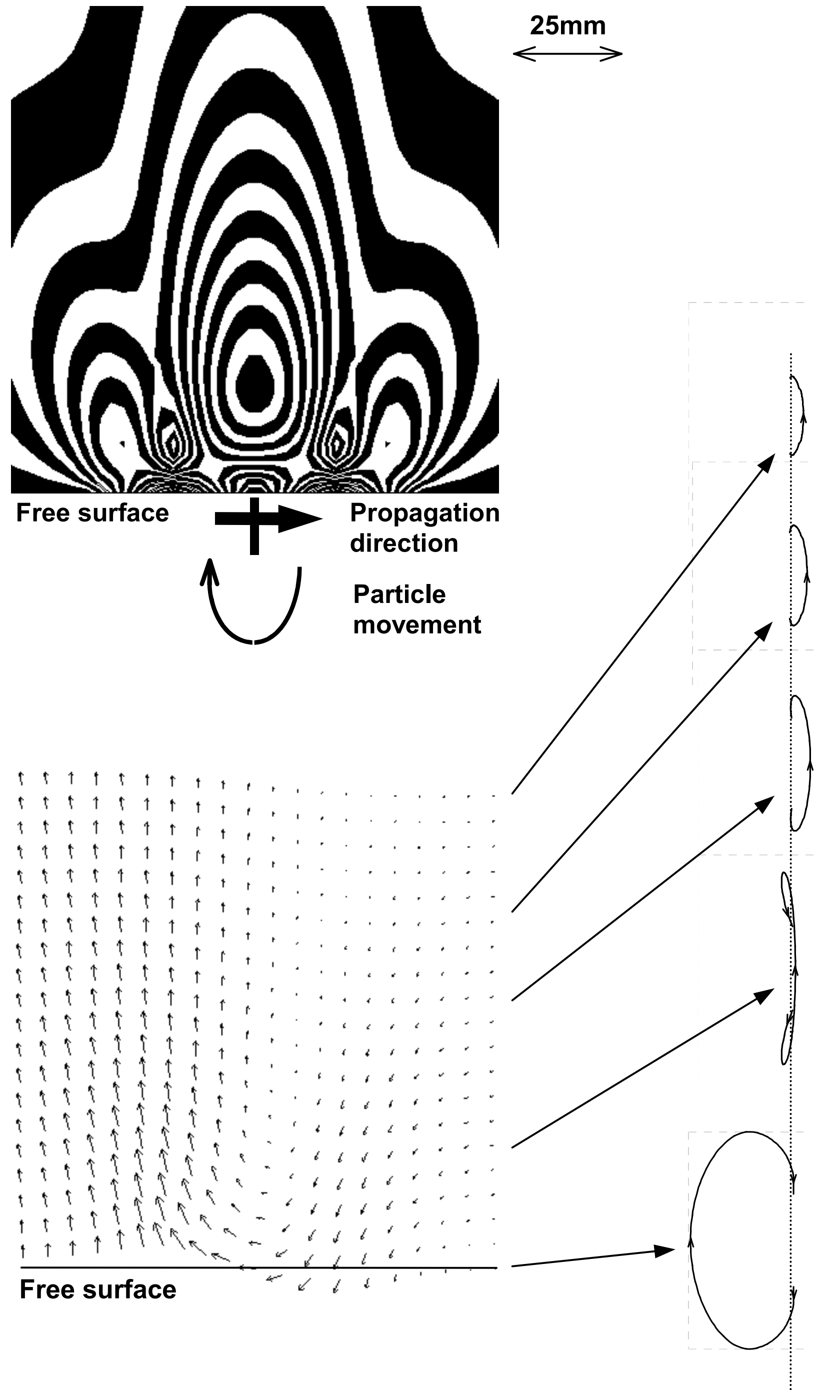

25mm
Free surface
Propagation direction
Particle movement
Free surface

Figure 1.

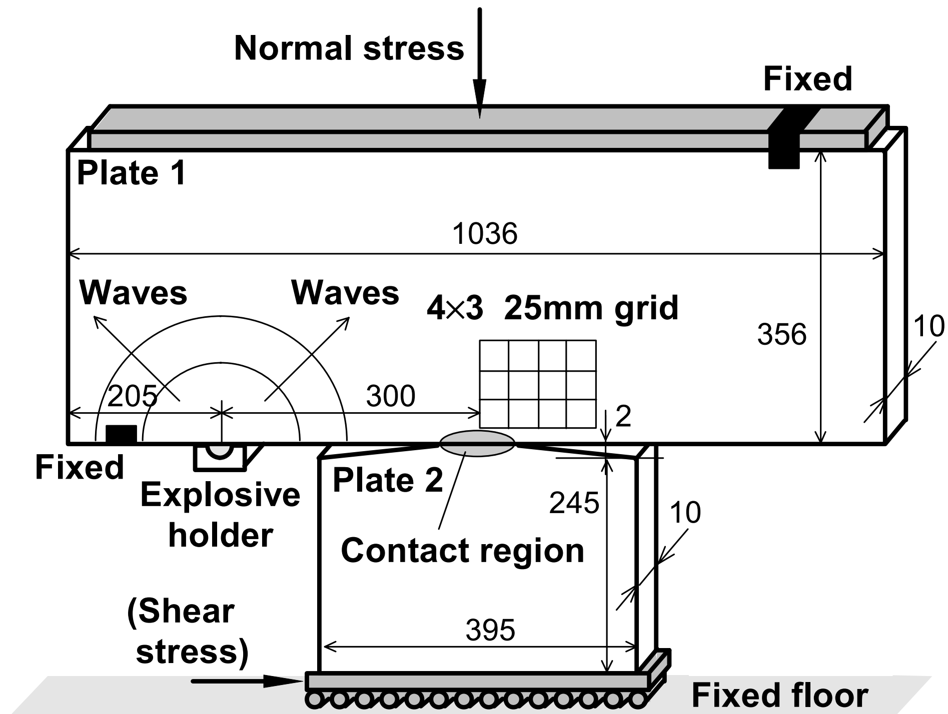
Normal stress
Fixed
Plate 1
1036
Waves
Waves
4×3 25mm grid
356
10
205
300
2
Fixed
Explosive holder
Plate 2
245
10
Contact region
(Shear stress)
395
Fixed floor

Figure 2.

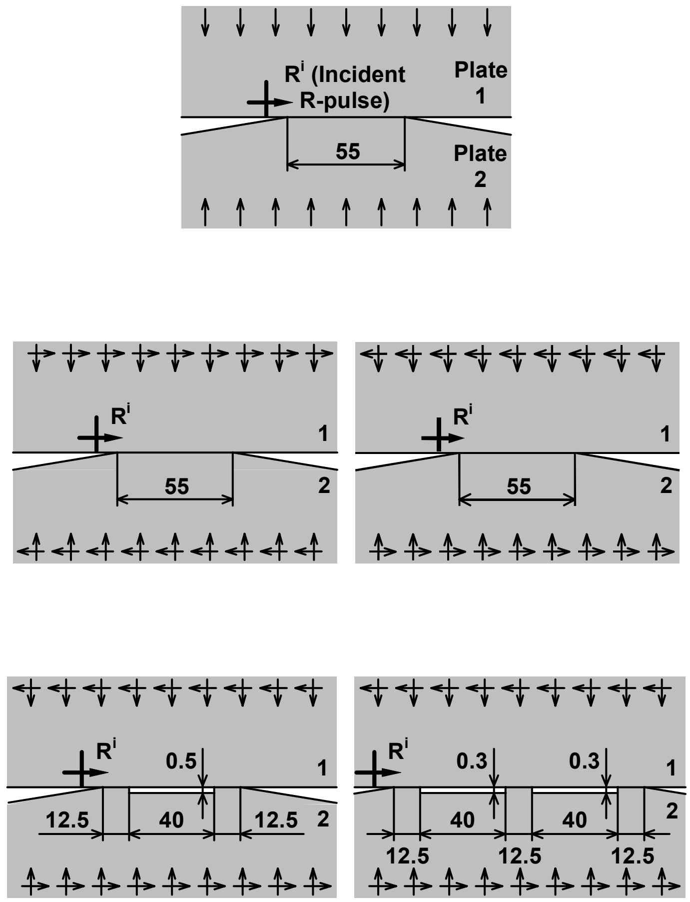

R^i (Incident
R-pulse)
Plate
1
55
Plate
2
R^i
1
55
2
R^i
1
55
2
R^i
0.5
1
12.5
40
12.5
2
R^i
0.3
0.3
1
40
40
2
12.5
12.5
12.5

Figure 3.

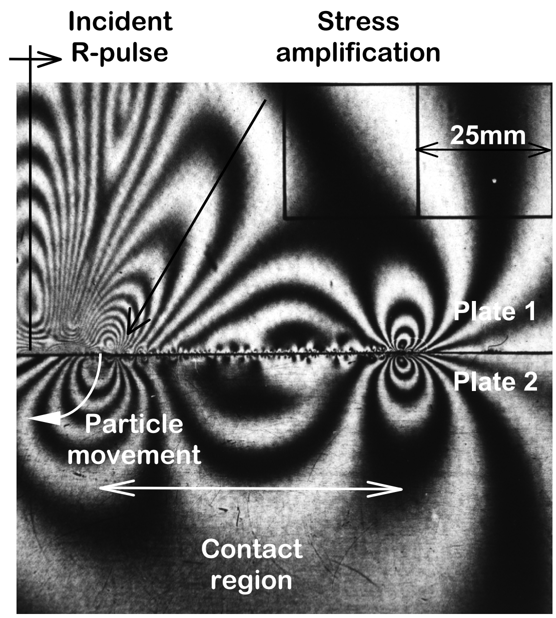
Incident
R-pulse
Stress
amplification
25mm
Plate 1
Plate 2
Particle
movement
Contact
region

Figure 4. (a)

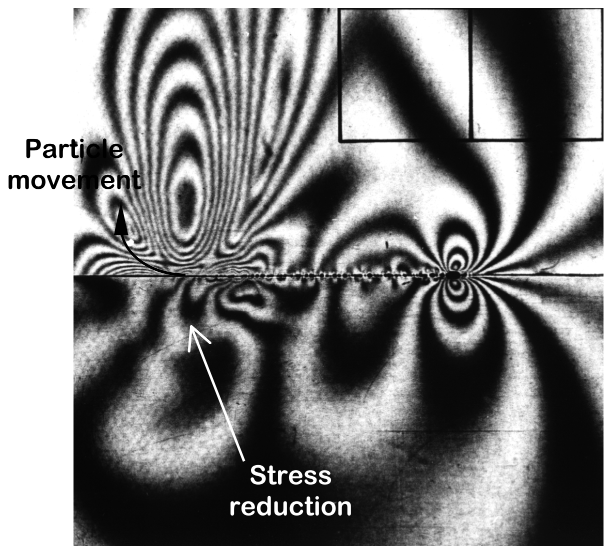

Figure 4. (b)

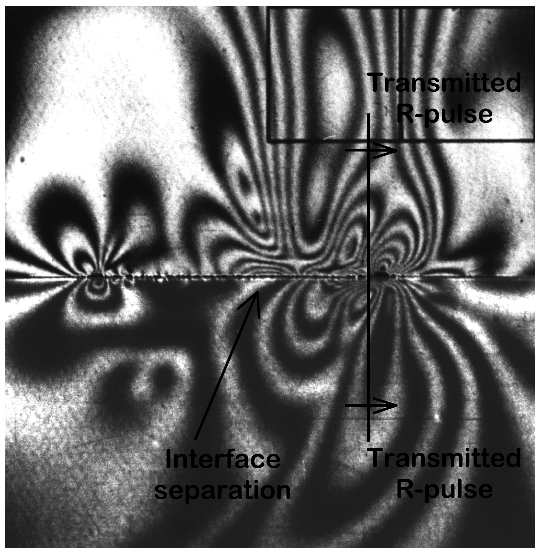
Transmitted
R-pulse
Interface
separation
Transmitted
R-pulse

Figure 4. (c)

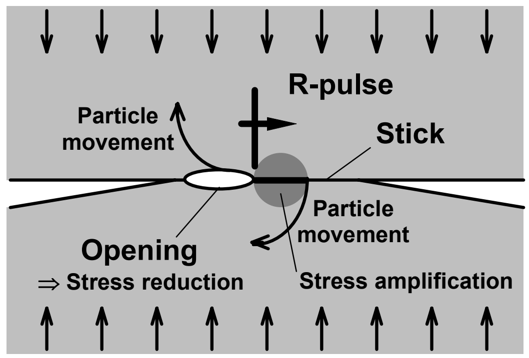
R-pulse
Particle
movement
Stick
Particle
movement
Opening
⇒ Stress reduction
Stress amplification

Figure 5.

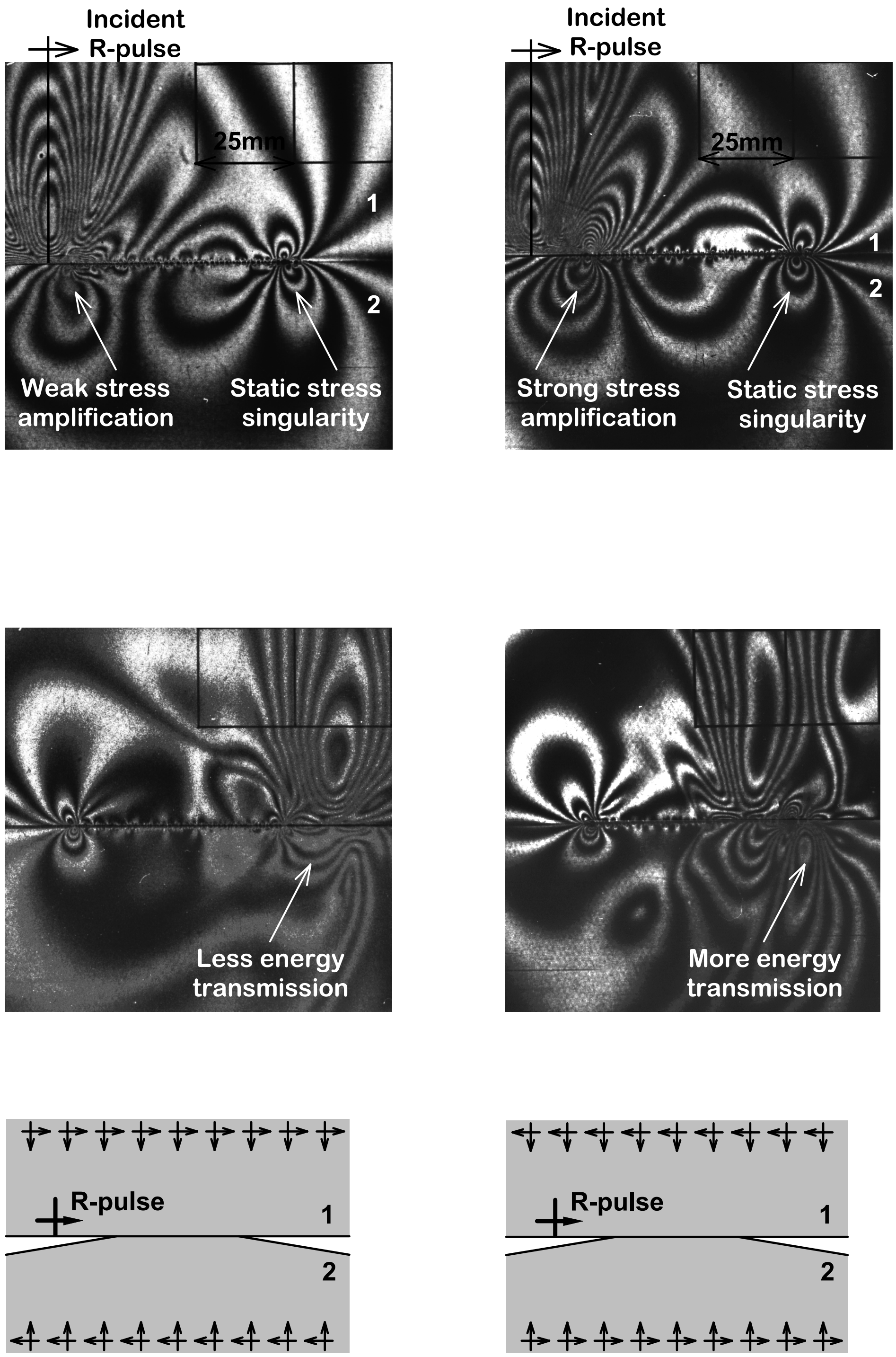
Incident
R-pulse
25mm
1
2
Weak stress
amplification
Static stress
singularity
Incident
R-pulse
25mm
1
2
Strong stress
amplification
Static stress
singularity
Less energy
transmission
More energy
transmission
R-pulse
1
2
R-pulse
1
2

Figure 6.

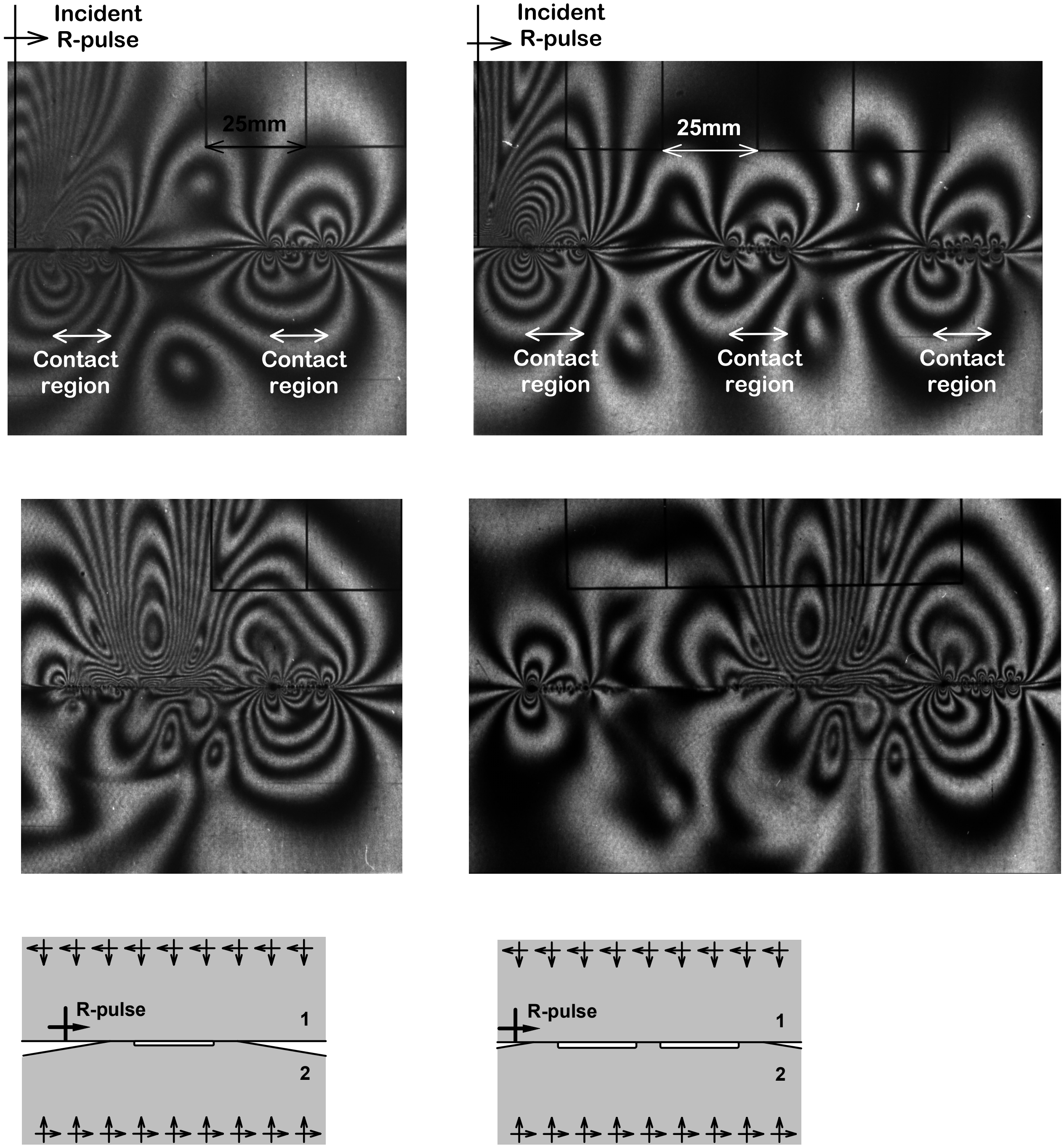
Incident
R-pulse
25mm
Contact
region
Contact
region
Incident
R-pulse
25mm
Contact
region
Contact
region
Contact
region
R-pulse
1
2
R-pulse
1
2

Figure 7.

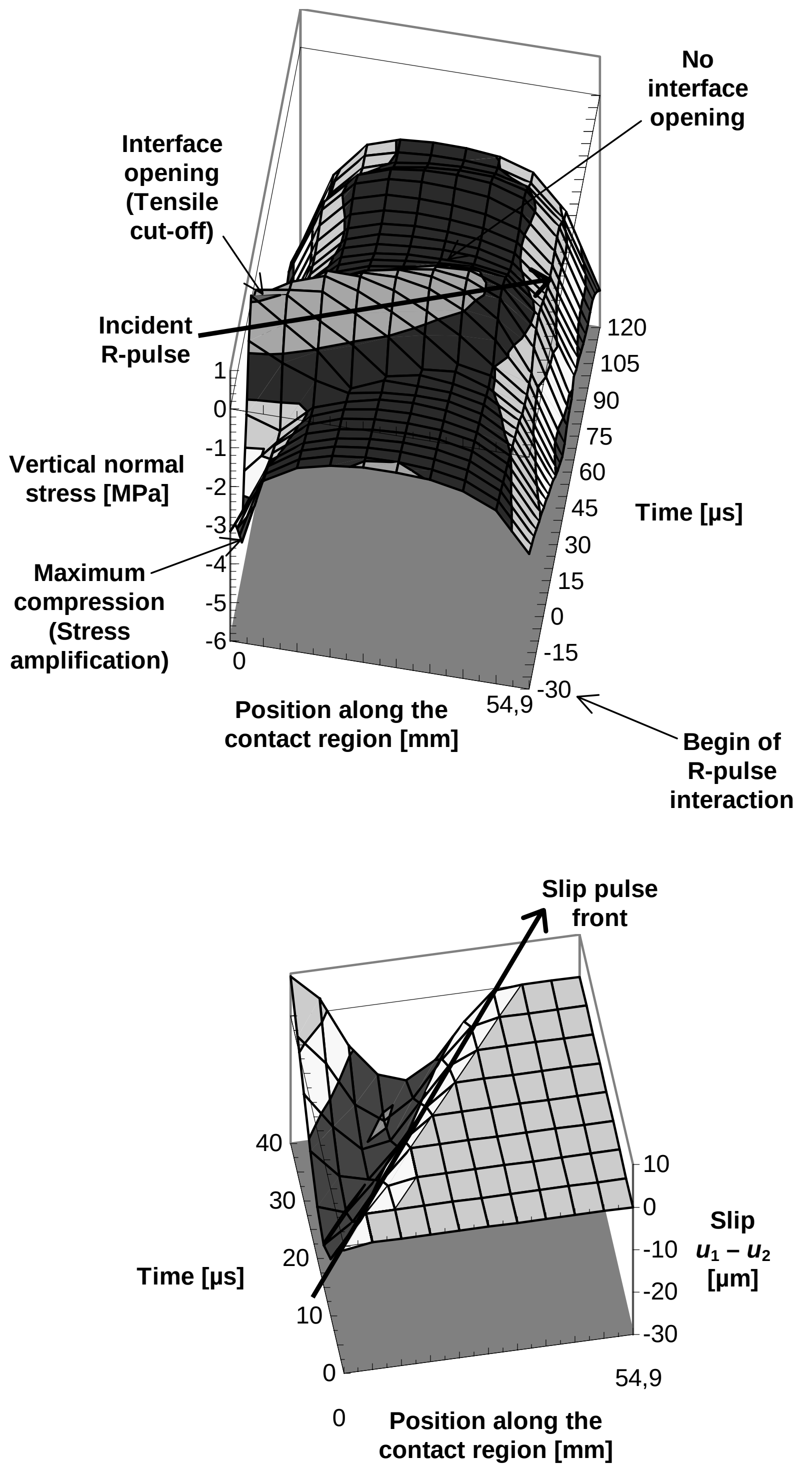
No
interface
opening
Interface
opening
(Tensile
cut-off)
Incident
R-pulse
Vertical normal
stress [MPa]
Maximum
compression
(Stress
amplification)
1
0
-1
-2
-3
-4
-5
-6
0
Position along the
contact region [mm]
54,9
120
105
90
75
60
45
30
15
0
-15
-30
Time [μs]
Begin of
R-pulse
interaction
Slip pulse
front
40
30
20
10
0
Time [μs]
0
Position along the
contact region [mm]
54,9
10
0
-10
-20
-30
Slip
$u_1 - u_2$
[μm]

Figure 8.

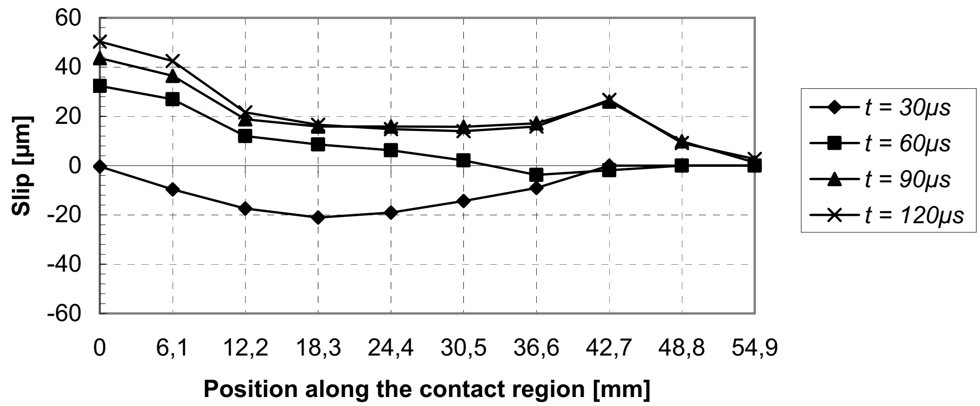
60
40
20
0
-20
-40
-60
Slip [µm]
0
6,1
12,2
18,3
24,4
30,5
36,6
42,7
48,8
54,9
Position along the contact region [mm]
t = 30µs
t = 60µs
t = 90µs
t = 120µs

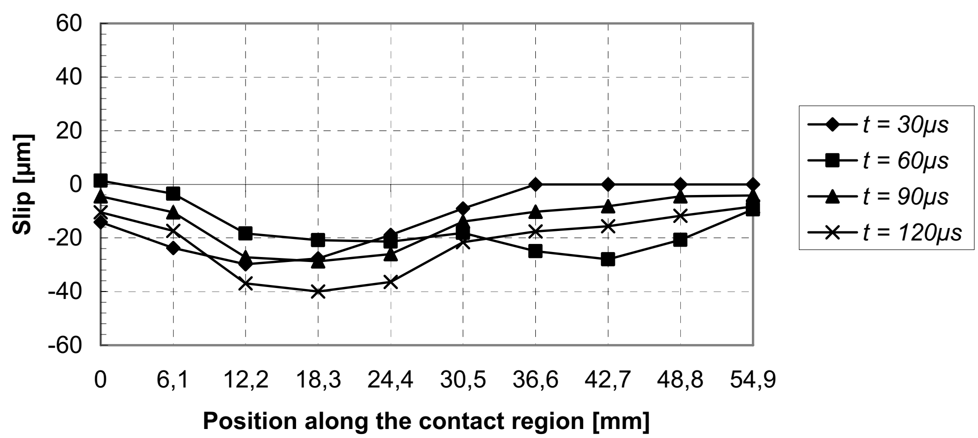
60
40
20
0
-20
-40
-60
Slip [µm]
0
6,1
12,2
18,3
24,4
30,5
36,6
42,7
48,8
54,9
Position along the contact region [mm]
t = 30µs
t = 60µs
t = 90µs
t = 120µs

Figure 9.

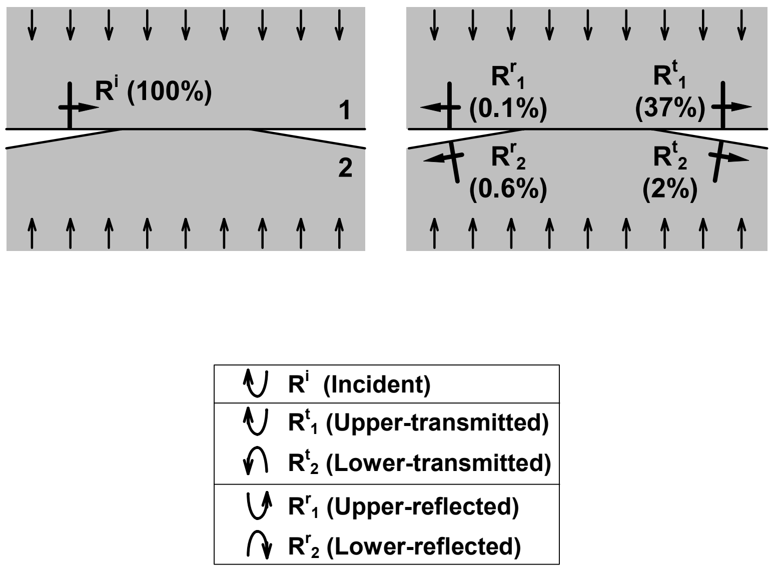

R^i (100%)
1
2
R^r_1 (0.1%)
R^t_1 (37%)
R^r_2 (0.6%)
R^t_2 (2%)
R^i (Incident)
R^t_1 (Upper-transmitted)
R^t_2 (Lower-transmitted)
R^r_1 (Upper-reflected)
R^r_2 (Lower-reflected)

Figure 10.

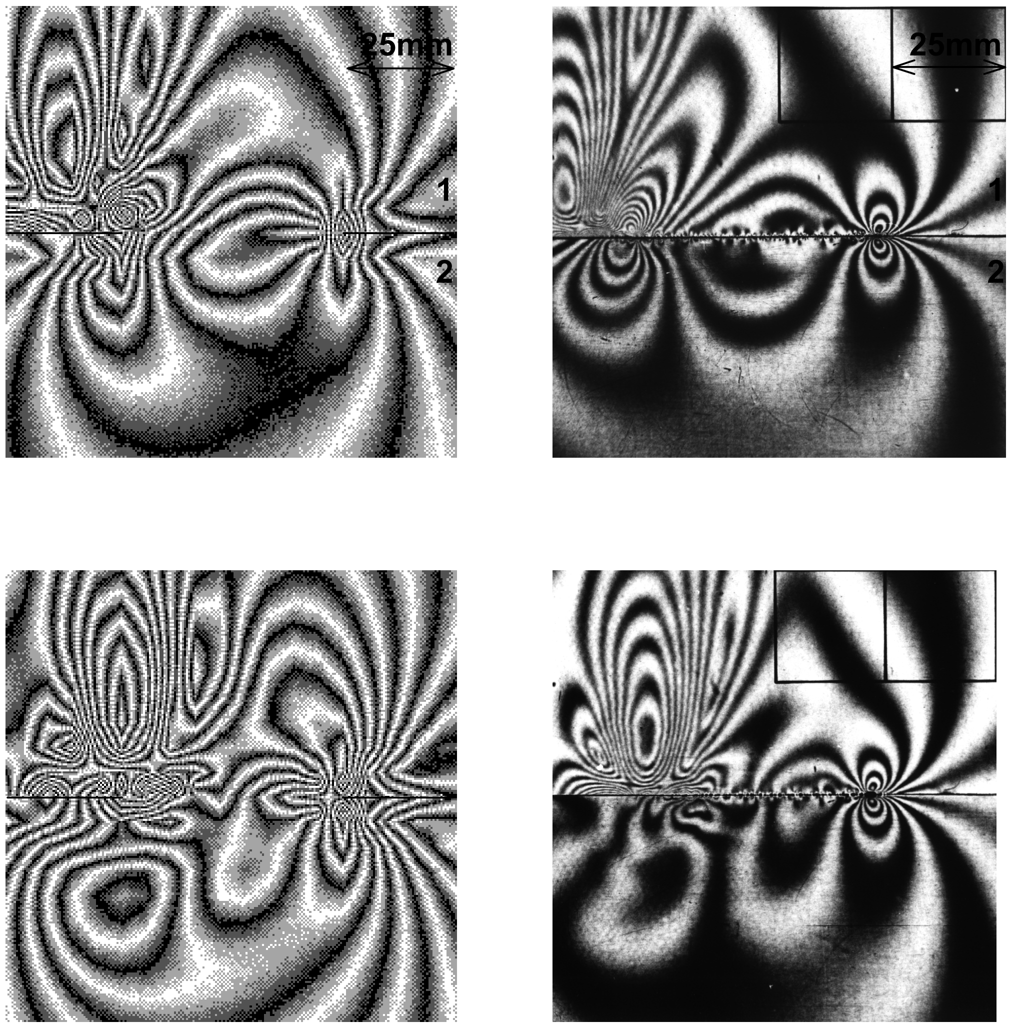

Figure 11.

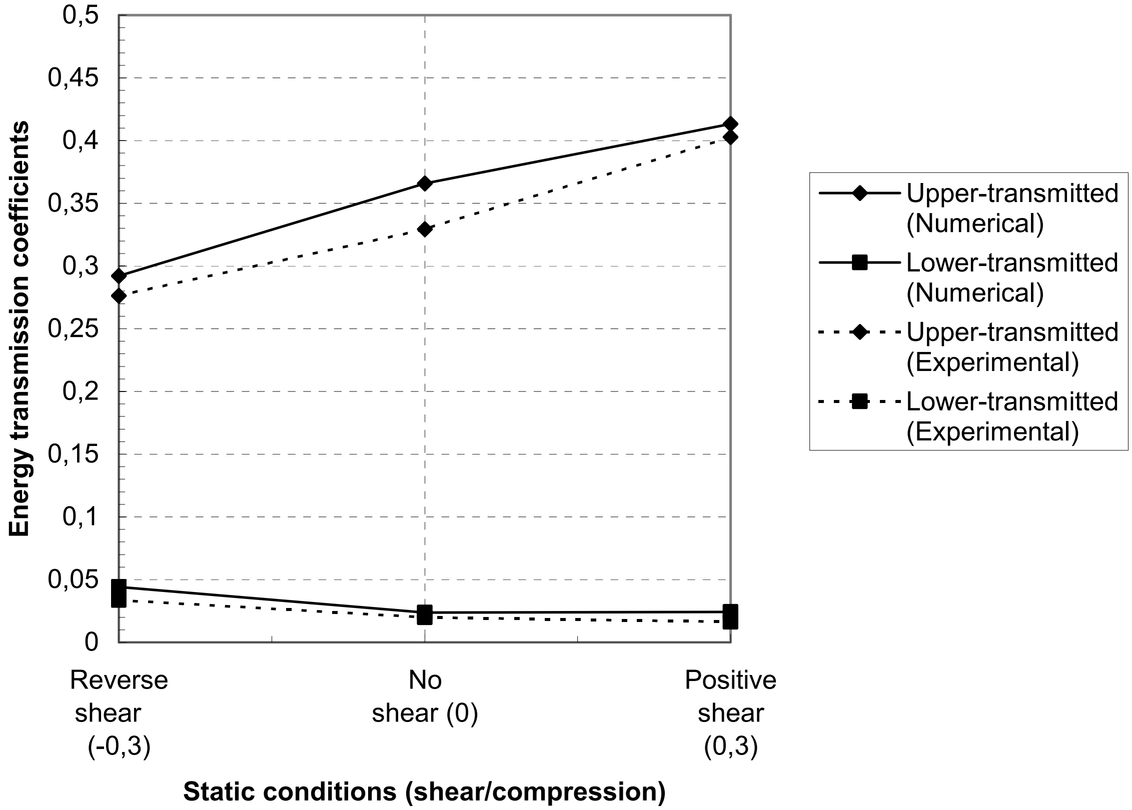

0,5
0,45
0,4
0,35
0,3
0,25
0,2
0,15
0,1
0,05
0
Energy transmission coefficients
Reverse shear (-0,3)
No shear (0)
Positive shear (0,3)
Static conditions (shear/compression)
Upper-transmitted (Numerical)
Lower-transmitted (Numerical)
Upper-transmitted (Experimental)
Lower-transmitted (Experimental)

Figure 12.

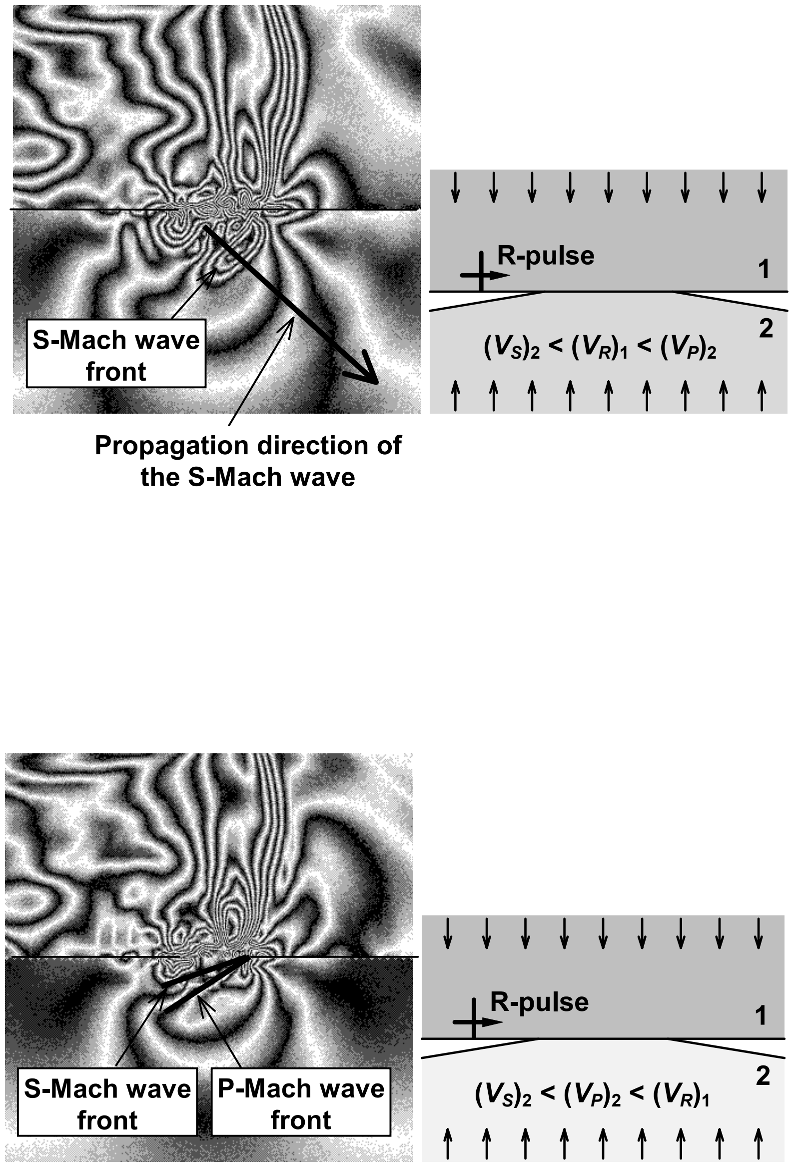
R-pulse
1
2
$(V_S)_2 < (V_R)_1 < (V_P)_2$
S-Mach wave front
Propagation direction of the S-Mach wave
R-pulse
1
2
$(V_S)_2 < (V_P)_2 < (V_R)_1$
S-Mach wave front
P-Mach wave front

Figure 13.

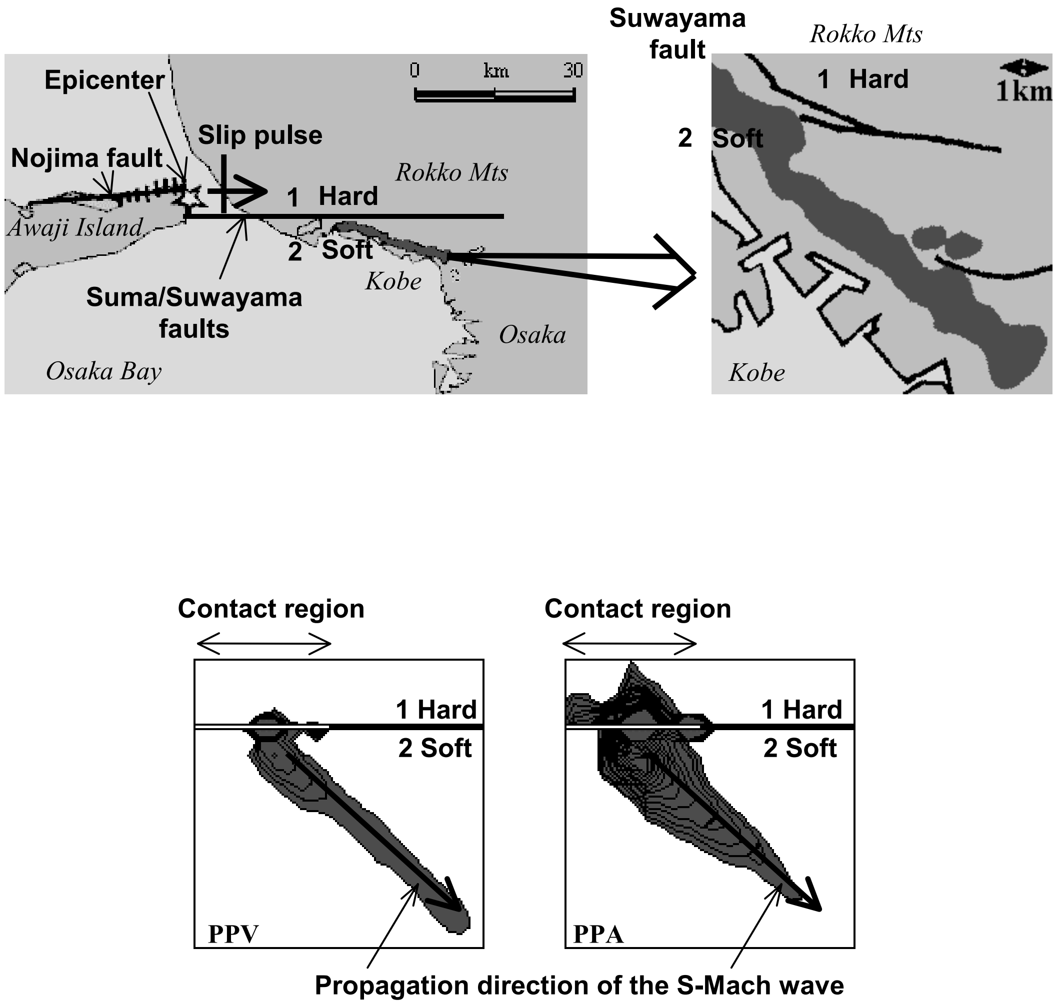
Epicenter
0
km
30
Slip pulse
Nojima fault
Rokko Mts
1 Hard
Awaji Island
2 Soft
Kobe
Suma/Suwayama
faults
Osaka
Osaka Bay
Suwayama
fault
Rokko Mts
1 Hard
1km
2 Soft
Kobe
Contact region
Contact region
1 Hard
2 Soft
1 Hard
2 Soft
PPV
PPA
Propagation direction of the S-Mach wave

Figure 14.